IEEE Open Journal of
Antennas and Propagation

Received 16 August 2023; revised 5 September 2023; accepted 13 September 2023. Date of publication 18 September 2023;
date of current version 6 October 2023.

Digital Object Identifier 10.1109/OJAP.2023.3316702

A Multi-Port Pattern Diversity Antenna With High Isolation

NGHIA NGUYEN-TRONG [1] (Senior Member, IEEE), AND CHRISTOPHE FUMEAUX [2] (Fellow, IEEE)

[1]School of Electrical and Mechanical Engineering, The University of Adelaide, Adelaide, SA 5005, Australia

[2]School of Electrical Engineering and Computer Science, The University of Queensland, Brisbane, QLD 4072, Australia

CORRESPONDING AUTHOR: N. NGUYEN-TRONG (e-mail: nghia.nguyentrong@adelaide.edu.au)

ABSTRACT A pattern-diversity antenna with 7 ports is proposed for multiple-input multiple-output (MIMO) applications. Orthogonal modes are utilized to achieve high isolation among all 7 ports in a relatively compact shared volume. As distinguishing feature from previous works, the concept of tripolarization is generalized, allowing to design antennas with a large number of orthogonal patterns in a single multi-port device. Based on this approach, a simple structure is proposed with only two printed circuit boards (PCB) separated by an air gap. The proposed multi-port antenna can provide a high degree of pattern and polarization diversity for the coverage of the whole upper hemisphere space. Measurements confirm the following results for the fabricated prototype: 7.7% impedance bandwidth, higher than 20 dB isolation among all ports with an antenna size of $(0.61^2 \times \pi \times 0.061)\lambda_L^3$ where λ_L is the free-space wavelength at the lowest operating frequency.

INDEX TERMS Pattern diversity, tri-polarized antennas, tripolarization, high isolation, low-profile antennas, MIMO antennas, monopolar antennas, orthogonal radiation patterns.

I. INTRODUCTION

MULTIPLE-INPUT Multiple-Output (MIMO) technology have become one of most crucial concepts in modern communications. In a MIMO system, the quality of communications channel, i.e., the channel capacity, can be significantly increased by appropriately combining the scattering signals due to multipath effects. Theoretically, this enhancement is multiplied with a greater number of antennas. The research in MIMO antennas may broadly be divided into two paths: (i) massive MIMOs, which contain a very large number of spatially distributed antennas (identical in most cases) with configurations similar to a large antenna array, (ii) MIMO antennas with a smaller number of ports in a single volume, for more compact devices such as drones, handheld devices, and small base stations. For the latter category, there is a vast literature on 2-4 port designs, mostly focusing on coupling reduction techniques. Within a constrained platform size, introducing more ports while keeping high isolation is extremely challenging. Most designs with more than four ports [1], [2], [3] exploit pattern diversity, i.e., arranging identical antenna elements such that their radiation maxima point in different directions.

One very interesting MIMO antenna development has been the tripolarized antenna concept [4], which was first proposed as an integration of three orthogonal dipoles, hence, the name "tri-pole". This type of antennas can provide three orthogonal radiation patterns with a theoretically infinite isolation in case a perfect symmetry is maintained. The tripolarized antennas in the literature have been developed based on the concept of three "physically" orthogonal radiators [5], [6], [7], [8] as similarly as in a tri-pole [4]. For applications with full ground plane, the antennas provide two orthogonal broadside modes and one omnidirectional mode with vertical polarization. These modes can be provided by a single dielectric resonator with a relatively high profile [9], [10]. Various radiating structures have been proposed for lower antenna profile [11], [12], [13], [14], [15], [16], [17] and/or wider operating bandwidth [18], [19], [20], [21], [22], [23]. Several designs were specifically targeted for different applications such as for Wireless Body Area Network (WBAN) [24], [25], retrodirective array [26], and vehicle-to-everything (V2X) communications [27].

This paper will extend the concept of tripolarized antennas by considering each "polarization" as an orthogonal

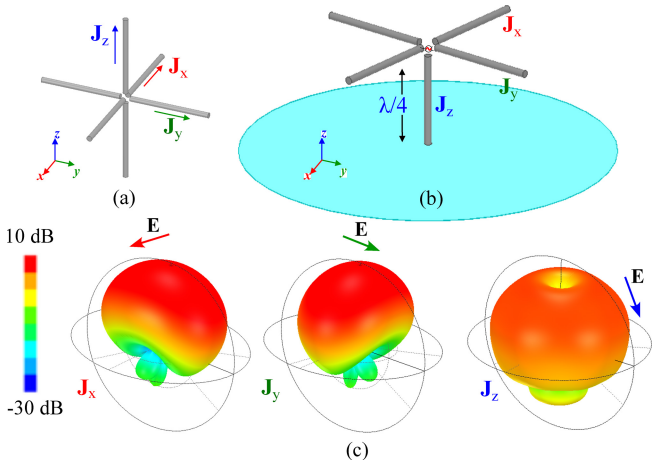

FIGURE 1. (a) Tri-polarized antenna original concept; (b) The design's adaptation for a large ground plane and (c) its typical 3D (co-polarization) radiation patterns. The 3D patterns for two broadside modes are represented in 3rd definition of Ludwig, Co-polar (X) and Co-polar (Y) - corresponding to J_x and J_y, respectively - while the 3D pattern for the omnidirectional mode represents the θ-component gain. The figure is adapted and modified from [23].

radiation pattern. From this perspective, different methods and techniques of multi-polarized antennas can be developed while maintaining the main advantage of the original/conventional tripolarized antennas, i.e., providing polarization/pattern diversity in a compact device.

The paper will first revisit the concept of tripolarized antennas with further discussion in Section II. Section III will demonstrate a three-port antenna with three orthogonal radiation patterns totally different from those of a conventional dipole-based tripolarized antenna. Finally, we demonstrate a 7-port MIMO antenna in Section IV with measurement results in Section V. In this final design, four ports are added to increase the pattern and polarization diversity. For these additional four ports, high isolation is obtained from both pattern orthogonalities and antenna spacing.

II. CONVENTIONAL TRIPOLARIZED ANTENNAS

Figure 1(a) shows the original concept of tripolarized antennas [4]. It consists of three orthogonal linear dipoles, all excited symmetrically from the center. For many applications where a ground plane is present, the concept may be represented as shown in Fig. 1(b) [23]. Here the electric current $\mathbf{J}_x$ and $\mathbf{J}_y$ are placed a distance of about a quarter-wavelength from the ground plane. The vertical dipole $\mathbf{J}_z$ is converted to a quarter-wavelength monopole on a ground plane. Several techniques have been proposed to reduce the antenna profile, ultimately creating a planar structure. These includes using artificial magnetic conductor (AMC) [20], replacing the monopole by a low-profile monopolar structure with shorting vias [12], [19], utilizing metasurfaces [21]. All the aforementioned designs share similar radiation patterns from each port as shown in Fig. 1(c). Mode 1 and Mode 2 produce two degenerated broadside patterns with orthogonal polarizations. Mode 3 excitation yields an omnidiretional pattern with vertical polarization, noting that the pattern is slightly conical in the upper half-space due to the finite ground plane.

It can be shown that the three patterns in Fig. 1(c) are orthogonal to each other. For clarification, two patterns are said to be orthogonal if their cross-correlation integrated over all angles is zero, i.e., $\rho_e = 0$ for [28]

$$\rho_e = \frac{\left|\int F_1(\theta,\phi) \bullet F_2(\theta,\phi) d\Omega\right|^2}{\int |F_1(\theta,\phi)|^2 d\Omega \int |F_2(\theta,\phi)|^2 d\Omega}. \quad (1)$$

where $\bullet$ denotes the Hermitian product. For antenna with 100% efficiency, the value of ρ_e can be calculated exactly from the S-parameters as proved in [29]

$$\rho_e = \frac{|S_{11}^* S_{12} + S_{21}^* S_{22}|^2}{\left(1 - \left(|S_{11}|^2 + |S_{21}|^2\right)\right)\left(1 - \left(|S_{22}|^2 + |S_{12}|^2\right)\right)}. \quad (2)$$

Equation (2) shows that a zero coupling between two ports of a lossless antenna, i.e., $S_{21} = 0$, implies that the two radiation patterns are orthogonal ($\rho_e = 0$). In various cases where the antenna structure and its excitations exhibit high degree of symmetry, zero coupling can be straightforwardly proved which leads to orthogonal patterns. A few examples are the odd and even modes in a cavity or the degenerated orthogonal modes (TM_{10} and TM_{01}) of a perfectly square patch.

Since all antenna designers are familiar with the terms "dual-polarized" or "dual-polarization", the terms tri-polarization suggests that another orthogonal polarization, e.g., along z-direction, is basically added as in a tri-pole antenna [4]. However, for any practical scenario, we may just view a tripolarized antenna as a radiator that can provide *three orthogonal radiation patterns* where the orthogonality is defined as in (1) for $\rho_e = 0$. The three orthogonal patterns do not necessarily need to be the same as those shown in Fig. 1(c). This perspective can inspire different methods to generalize the concept and construct various types of MIMO antennas with multiple orthogonal radiating modes with high purity, thus allowing to keep a high isolation among all ports.

III. TWO AND THREE-PORT DESIGNS WITH ORTHOGONAL OMNIDIRECTIONAL TOTAL POWER PATTERNS

In this section, we will demonstrate a new three-port antenna with three orthogonal patterns but different from those of a conventional tripolarized antenna. These patterns all have omnidirectional *total* radiated field (corresponding to power or amplitude pattern).

A. TWO-PORT DESIGN

We can consider the structure shown in Fig. 2, which consists of two conductive rings printed on two substrates (Rogers Duroid 5880, relative permittivity of $\epsilon_r = 2.2$, loss tangent $\tan\delta = 0.0009$) separated by an air gap of $h_a = 5$ mm. The substrate thicknesses are $h_1 = 1.578$ mm and $h_2 = 0.787$ mm, respectively. The bottom ring is excited using two probe feeds while the top ring acts as a parasitic

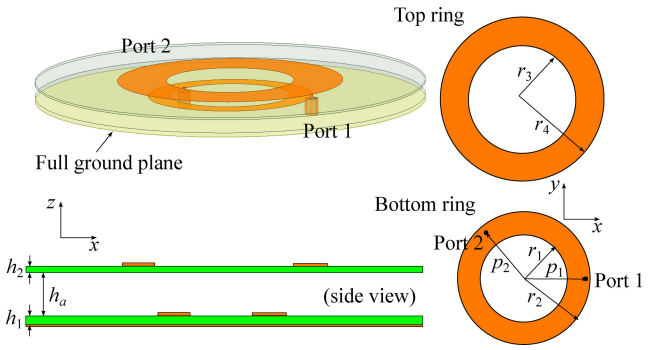

FIGURE 2. (a) A dual-port antenna with orthogonal radiation patterns. The optimized parameters are $r_1 = 22.5$, $r_2 = 31$, $r_3 = 24$, $r_4 = 42.5$, $h_1 = 1.578$, $h_2 = 0.787$, $h_a = 5$ (unit: mm). Note: The inner pin of the SMA connectors are attached to the bottom ring.

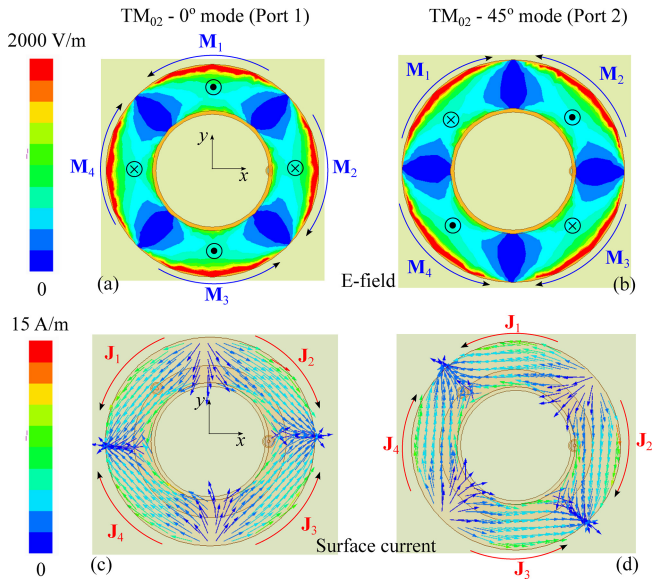

FIGURE 3. Simulated electric field (first row) and surface current (second row) on the top layer of the antenna in Fig. 2. Left column: TM_{02}-0° mode, Right column: TM_{02}-45°.

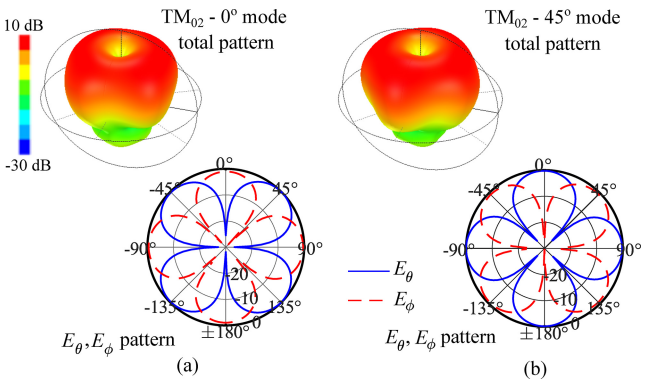

FIGURE 4. Simulated 3D total patterns and 2D normalized patterns in $\theta = 45°$-plane for (a) $TM_{02} - 0°$ mode and (b)$TM_{02} - 45°$ mode excitation of the antenna in Fig. 2.

element that can extends the bandwidth. It is noted that this structure was first used in [30], however, the modes and their corresponding radiation patterns, which are quite interesting and unique, were not fully analyzed and described. The S-parameters of the antenna in Fig. 2 are the same as in the 3-port design in Section III-B (for Port 1 and Port 2) and are not shown here fore brevity.

This double-ring structure can be excited with higher-order modes of both rings, i.e., TM_{02}-0° and TM_{02}-45° (see the electric field vector and surface electric current in Fig. 3). The name of the mode is explained as follows: they are TM (transverse magnetic) mode because the magnetic field vector is perpendicular to the assumed broadside direction (z-axis); the first index, i.e., 0, indicates that there is no variation in radial direction (in cylindrical coordinates); the second index, i.e., 2, indicates the number of cycle variations along the azimuthal ϕ-direction, the angle (0° or 45°) indicates the ϕ-angle that gives the maximum of electric field. This angle is required to distinguish between these two degenerated modes. They are orthogonal to each other, which results in very high isolation between the two antenna ports.

Let us now examine the radiation pattern resulting from these two modes (Fig. 4). First, the 3D total gain (or power) patterns of both modes are omnidirectional and appear similar to Mode 3 in Fig. 1(c). However, they are in fact different when considering angular variations of polarization, which was not discussed in [30]. Figure 4 also shows the 2D pattern for the two orthogonal components (E_θ and E_ϕ) in a constant θ-plane (at the maximum radiation direction $\theta = \theta_{\max} = 45°$). It can be observed that there are nulls in each of the E_θ or E_ϕ patterns, which make the patterns essentially different from the pattern of a monopole. Thus, they should not be characterized as omnidirectional patterns. Nevertheless, since the total gain is almost constant with respect to ϕ, the pattern might only be referred as omnidirectional total power pattern (or *total pattern* in short).

The radiation patterns in Fig. 4 are quite interesting and are worth a theoretical explanation. The ring at the TM_{02}-0° mode resonance can be considered as a superposition of quadrupolar electric currents and magnetic currents as shown in Fig. 3. The direction of the 4 equivalent magnetic currents $\mathbf{M}_i$ is obtained from the field equivalence principle. Considering the direction $\phi = 0°$, the E_ϕ-component contributions from the radiated field of the 4 electric current $\mathbf{J}_i$ are totally canceled out due to the perfect destructive interference from two pairs of electric currents ($\mathbf{J}_2$, $\mathbf{J}_3$) and ($\mathbf{J}_1$, $\mathbf{J}_4$). However, there are constructive interferences from the equivalent magnetic currents $\mathbf{M}_2$ and $\mathbf{M}_4$ for the E_θ-component in the direction $\phi = 0°$. Similarly, considering the direction $\phi = 45°$, the θ-component of the radiated E-field from the 4 magnetic currents $\mathbf{M}_i$ are totally canceled out due to the perfect destructive interference from two pairs of equivalent magnetic currents ($\mathbf{M}_2$, $\mathbf{M}_3$) and ($\mathbf{M}_4$, $\mathbf{M}_1$). Based on the electric field distribution, it can be shown that these equivalent magnetic currents are 45° offset by the electric currents. Thus, for the TM_{02}-0° mode, E_θ-pattern shows 4 nulls at $\phi = 45°, 135°, 225°, 315°$ and E_θ-pattern shows 4

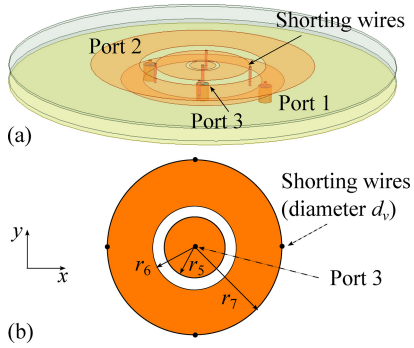

FIGURE 5. (a) 3D transparent view, (b) planar representation of the three-port design with three orthogonal omnidirectional total patterns. Substrate arrangement, top and bottom rings are the same as in Fig. 2. The optimized parameters are $r_5 = 5$, $r_6 = 6.4$, $r_7 = 18$, and $d_v = 1$ (unit: mm).

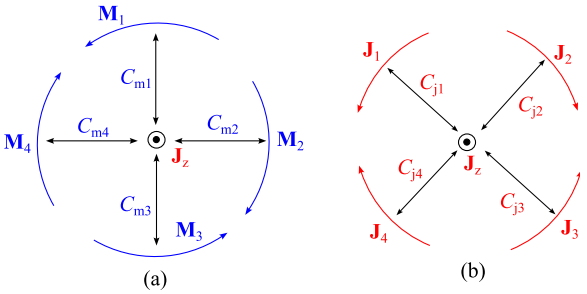

FIGURE 6. Fields from Port 1 and coupling to the center Port 3 due to (a) equivalent magnetic currents and (b) surface electric currents.

nulls at $\phi = 0°, 90°, 180°, 270°$. Similar explanation can be applied for the TM_{02}-45° mode.

In summary, the radiation patterns in Fig. 4 are consistent with the electric and (equivalent) magnetic current distributions shown in Fig. 3. Due to the inconsistency in the polarization of a single pattern in azimuthal direction, this type of radiation patterns might be not useful for point-to-point communications. However, they are well-suited for MIMO applications in a rich scattering environment. Furthermore, the nulls in the patterns may be used for tracking or angle-of-arrival estimation, which is beyond the scope of this paper.

B. THREE-PORT DESIGN

The design in Fig. 2 is now modified to add a port at its center to excite the vertically polarized omnidirectional mode of a top-loaded planar monopole [31], [32]. The design is shown in Fig. 5. Apart from the added planar monopole, all other design parameters are the same as in Fig. 2. A ring gap is used to improved the impedance matching and four shorting wires are used at the patch periphery to lower the resonance frequency [33]. This structure is equivalent to a magnetic current loop or a vertical electric current (monopole) at the rings common center.

1) PROOF OF ORTHOGONALITY

Figure 6 shows the radiation sources when exciting Port 1 and Port 3. For easy visualization, the groups of electric currents and equivalent magnetic currents are separated into 2 subfigures. The coupling from Port-1 and Port-3 can be written as a complex sum

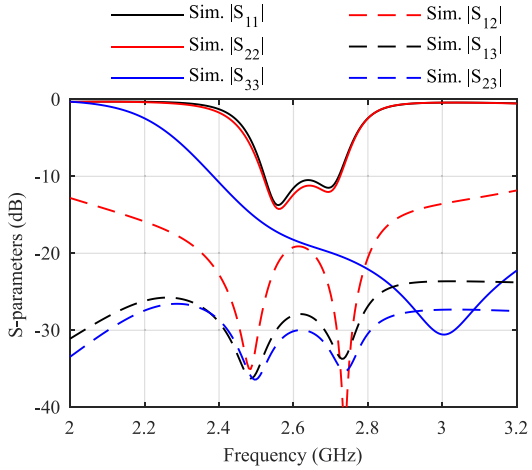

FIGURE 7. Simulated S-parmeters of the 3-port antenna design in Fig. 5.

$$C = \sum_{i=1}^{4} C_{mi} + \sum_{i=1}^{4} C_{ji} \tag{3}$$

where C_{mi} and C_{ji} are the coupling coefficients from each of the current source $\mathbf{M}_i$, $\mathbf{J}_i$, respectively, produced by the excitation of Port 1 to the center vertical current source $\mathbf{J}_z$ of Port 3. Due to symmetry and the anti-phase feature of the current sources $\mathbf{M}_i$, $C_{m1} = -C_{m2}$ and $C_{Cm3} = -C_{m4}$ and therefore $\sum C_{mi} = 0$. Same arguments can be applied for the set of 4 electric currents, as shown in Fig. 6(b). Thus, $\sum C_{ji} = 0$ and $C = 0$. Theoretically, the coupling between Port-1 and Port-3 is zero due to symmetry considerations if a pure mode TM_{02}-0° is excited. This also applies for the coupling between Port-2 (TM_{02}-45° mode) and Port-3.

Figure 7 shows the reflection coefficients and couplings among all ports. For Port-1 and Port-2, there are two resonances corresponding to the TM_{02} mode associated with the excitation (bottom) ring and the parasitic (top) ring. It can be observed that the coupling $|S_{12}|$ has deep minima at these two frequencies. This is evidence that the modes are highly pure on resonances, which yield a near perfect symmetry. The coupling increases in the middle of the band (about 2.6 GHz) as perfect symmetry is no longer maintained.

The coupling from Port 3 to either Port 1 or Port 2 is also very low at around −30 dB in the operating band. Two minima of the coupling also occur at the resonance frequency of each ring. The results indicate an important feature: high isolation is often associated with the symmetry of the structure.

2) RADIATION PATTERN

The simulated 3D gain G_θ, G_ϕ patterns for each port are summarized in Fig. 8. These three radiation patterns are orthogonal to each other with very low coupling among

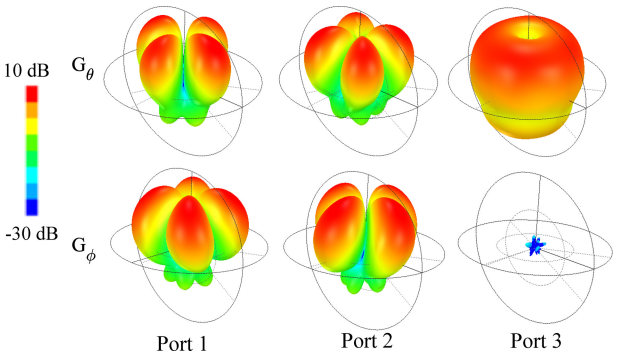

FIGURE 8. Simulated 3D gain patterns of the 3-port antenna design in Fig. 5.

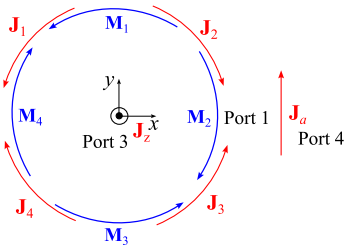

FIGURE 9. The concept of adding 4th port.

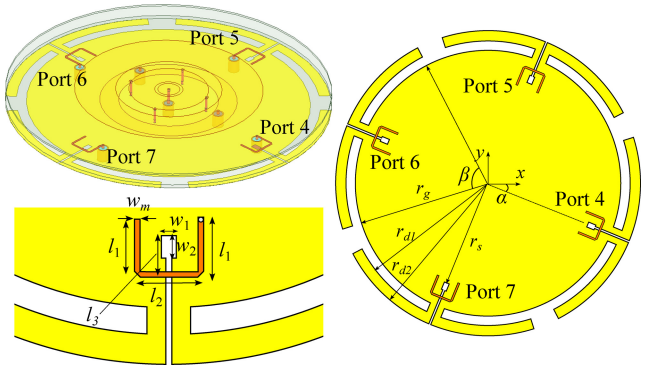

FIGURE 10. Final antenna design by adding 4 additional ports. The three-port antenna structure is exactly the same as in Fig. 5. The optimized parameters are $w_1 = 2.5$, $w_2 = 3.75$, $w_m = 0.925$, $l_1 = 9.23$, $l_2 = 10.65$, $l_3 = 6.23$, $r_s = 52$, $r_g = 64$, $r_{d1} = 68.5$, $r_{d2} = 73.5$ (unit: mm) and $\beta = 80°$.

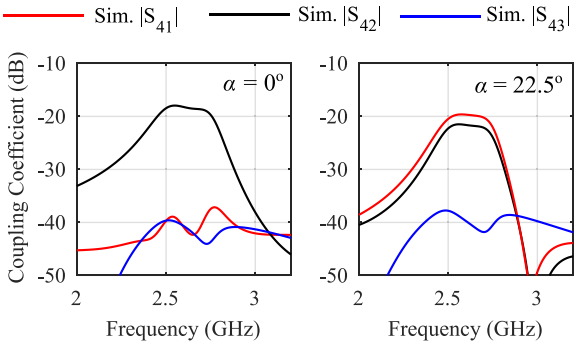

FIGURE 11. Simulated coupling from Port 4 to Port 1, 2, 3 for two cases $\alpha = 0°$ (no rotation as in Fig. 9) and $\alpha = -22.5°$ (as in final realization in Fig. 10).

all excitation ports, similarly to a conventional tripolarized antenna. Perfect orthogonality can be achieved with differential feeding, however at the cost of a more complicated feeding network. As an aside, we note that higher-order modes are utilized here, as this will provide a means to extend the concept of tri-polarization and to add more ports in the design as will be shown in the next section.

IV. ADDING MORE PORTS

At this point, a natural question may be raised: Is it possible to add an omnidirectional patterns with *horizontal polarization*? This would correspond to patterns as for Port 3 in Fig. 8 but with G_θ and G_ϕ being switched. Indeed, this pattern is also mutually orthogonal with all three patterns shown in Fig. 8. The dual omnidirectional patterns can be found in literature such as [34], [35], [36], [37], [38], [39]. Another observation from Fig. 8 is that the upper hemisphere is not fully covered yet. The three-port design in Section III can provide high polarization diversity in the angle $\theta \approx 30°$ to $60°$ (due to the conical nature of the patterns from Port 1 and Port 2). When approaching $\theta = 90°$, the monopolar pattern from Port 3 can provide coverage with vertical polarization. Besides, the broadside direction ($\theta = 0°$) is not covered by any port. Thus, in this section, we will show a design that solves all of the above issues with full polarization diversity covering the whole upper hemisphere. It should be emphasized the following result is not achievable in the conventional tripolarized antenna.

First, we consider exciting an electric current $\mathbf{J}_a$ (Port 4) whose phase center is along the $\phi = 0°$ direction, i.e., on the x-axis (see Fig. 9). This electric current lies on the horizontal xy-plane with the direction along the y-axis. The coupling between Port 3 and Port 4 is bound to be very low due to their orthogonal polarization, as this represents the case of having two orthogonal dipoles at some distance. For the coupling from Port 1 to Port 4, we can first neglect the interaction with the equivalent magnetic currents $\mathbf{M}_i$ as these also have orthogonal polarization compared to $\mathbf{J}_a$. Due to symmetry and the anti-phase nature of $\mathbf{J}_i$, the couplings from $\mathbf{J}_a$ to $\mathbf{J}_2$ and $\mathbf{J}_3$ cancel each other (similarly for $\mathbf{J}_1$ and $\mathbf{J}_4$). Thus, theoretically, when perfect symmetry is maintained, the couplings from Port 4 to Port 1 and Port 3 are zero. However, due to the 45° rotation, the coupling from Port 2 to Port 4 is not zero. Thus, a tradeoff can be made by rotating the current $\mathbf{J}_a$ by either 22.5° or −22.5°. Finally, 3 more ports can be added by rotating $\mathbf{J}_a$ by 90°, 180° and 270°.

The concept in Fig. 9 is realized as shown in Fig. 10. Four horizontal electric dipoles are added, corresponding to Port 4-7 excitation. This group of dipoles is rotated by an angle $\alpha = -22.5°$ with respect to the x-axis. Figure 11 shows the coupling from Port 4 to Port 1, 2, 3 for $\alpha = 0°$ and $\alpha = -22.5°$. For the case $\alpha = 0°$, the coupling from Port 4 to Port 1 and Port 2 is very small (about −40 dB), which agrees with the theoretical explanation above. However $|S_{42}|$ is high (about −18 dB). By making a tradeoff between $|S_{42}|$ and $|S_{41}|$ with $\alpha = -22.5°$, the values of $|S_{42}|$ and $|S_{41}|$

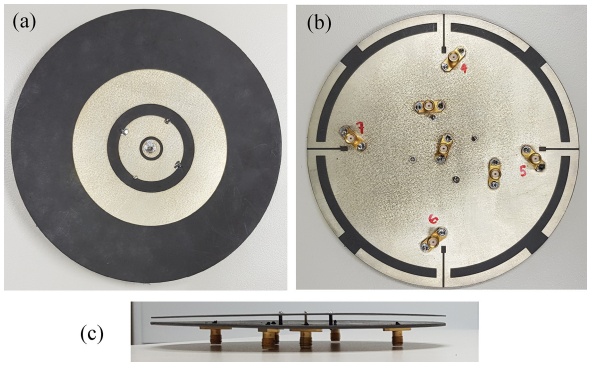

FIGURE 12. Photograph of the fabricated prototype: (a) top view and; (b) bottom view; (c) side view.

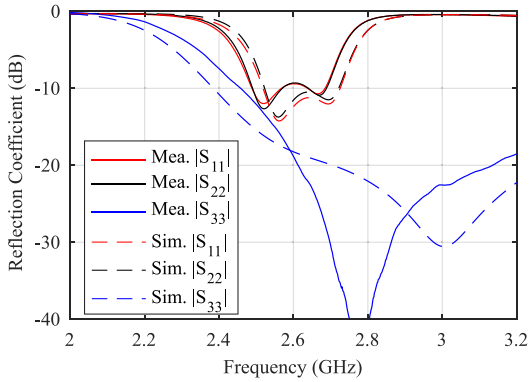

FIGURE 13. Reflection coefficients at Port 1, 2 and 3.

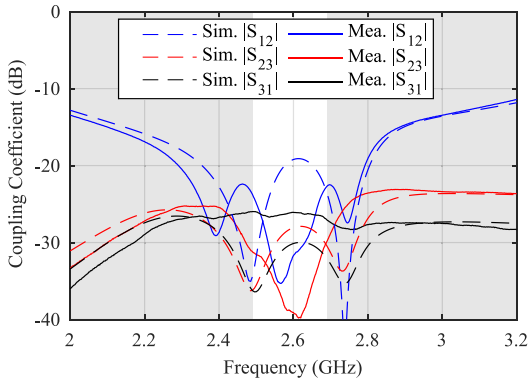

FIGURE 14. Coupling coefficients among port 1, 2 and 3. The highlighted central part is the overlapped impedance bandwidth provided by Port 1, 2, and 3.

become similar and reach a level of nearly −20 dB (or better).

With the presence of the ground plane, each dipole will radiate with a horizontally polarized broad beam towards the direction it is pointing to, i.e., $\phi = -22.5°, 67.5°, 157.5°, 247.5°$ in the $\theta = 90°$ plane. This arrangement enables the coverage of all directions in the upper hemisphere. For each direction, dual-polarization is available from at least 4 ports, providing a great diversity in pattern and polarization. Furthermore, the isolation from all ports are all better than approximately 20 dB in simulation (which will be confirmed by measurement later).

Finally, if all four ports 4-7 are excited with the same phase and same magnitude then a horizontally polarized omnidirectional pattern can be achieved as demonstrated in [37].

V. ANTENNA MEASUREMENT AND RESULTS

The optimized 7-port antenna introduced in Section IV has been fabricated and measured to validate the proposed concept. A photo displaying the top and bottom view of the fabricated prototype is shown in Fig. 12. This section will summarize the simulated and measured of S-parameters, radiation patterns, gain and efficiency of the antenna.

A. S-PARAMETERS

First, Fig. 13 plots the results for the reflection coefficients at Port 1, 2 and 3. In general, reasonable agreement between simulation and measurement is obtained. A minor shift (about 1.5%) in the operating frequency range and a slight degradation in $|S_{11}|$ and $|S_{22}|$ levels are observed. Those effects are due to a possible mechanical inaccuracy in the gap between the two substrates, the fabrication tolerance and the variation of substrate properties including its permittivity and thickness. A very minor beach of the condition $|S_{nn}| < -10$ dB occurs at 2.6 GHz (about −9.3 dB). Full-wave simulation indicates that this issue can be solved by slightly adjusting the air gap h_a. As expected, reflection coefficients for Port 1 and 2 are almost identical while Port 3 shows a much wider bandwidth, which is typical for a low-profile monopolar antenna with shorting wires [31]. The overlapped operating bandwidth is from 2.49 to 2.69 GHz, i.e., corresponding to 7.7% fractional bandwidth.

The coupling coefficients among Port 1, 2 and 3 are shown in Fig. 14. As expected, the coupling coefficients from Port 3 to either Port 1 or Port 2 are quite low (less than −26 dB) due to their orthogonal patterns. The coupling between Port 1 and Port 2 shows some local minima, which corresponds to the frequencies where nearly pure orthogonal modes are excited at Port 1 and Port 2. Overall, the measured isolation is better than 22 dB across the operating bandwidth.

The reflection coefficients for Port 4, 5, 6 and 7 excitation are shown in Fig. 15. Ports 4-7 show almost identical reflection coefficients as expected since they are basically identical antennas pointing in different directions. The impedance bandwidth for Ports 4-7 covers the overlapped bandwidth of Port 1-3. Thus, the overall overlapping bandwidth of all ports is from 2.49 to 2.69 GHz.

The coupling coefficients from Port 4 to Port 1-3 are shown in Fig. 16. The coupling coefficients from Port 5, 6 or 7 to Port 1-3 are similar and are not shown here for brevity. Very good agreement with simulation is obtained. Finally, the coupling among Port 4-7 are also shown in Fig. 17. Due to symmetry, we only need to show to coupling from Port 4 to Port 5, 6 and 7. High isolation of better than 20 dB is obtained as predicted by full-wave simulations. It

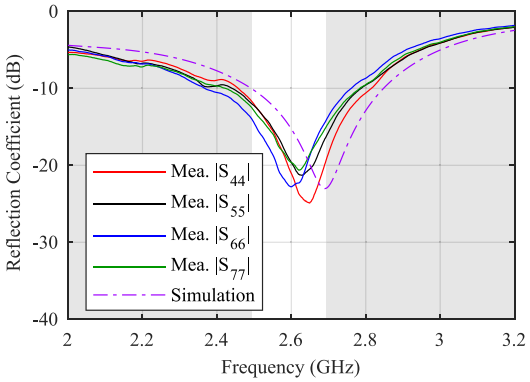

FIGURE 15. Reflection coefficients at Port 4, 5, 6 and 7. The simulation results are identical for all of these ports. The highlighted central part is the overlapped impedance bandwidth provided by Port 1-3.

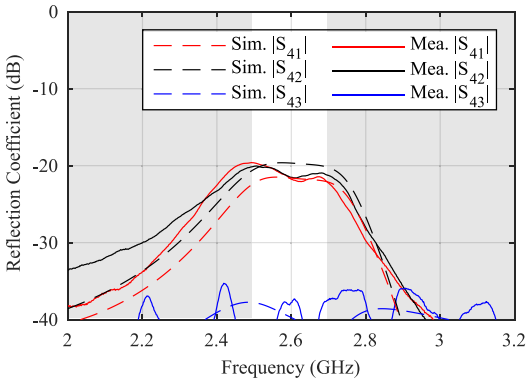

FIGURE 16. Coupling coefficients from Port 4 to Port 1, 2, 3. The highlighted central part is the overlapped impedanced bandwidth provided by Port 1, 2, 3.

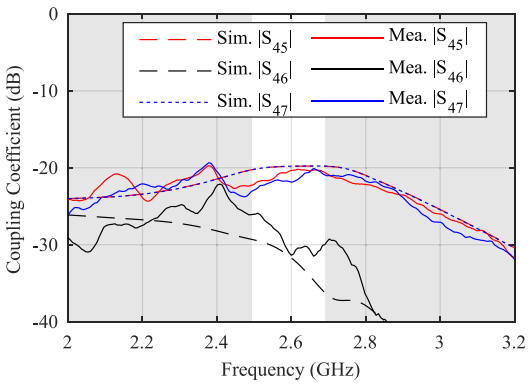

FIGURE 17. Coupling coefficients from Port 4 to Port 5, 6, 7. The highlighted central part is the overlapped impedance bandwidth provided by Port 1, 2, 3.

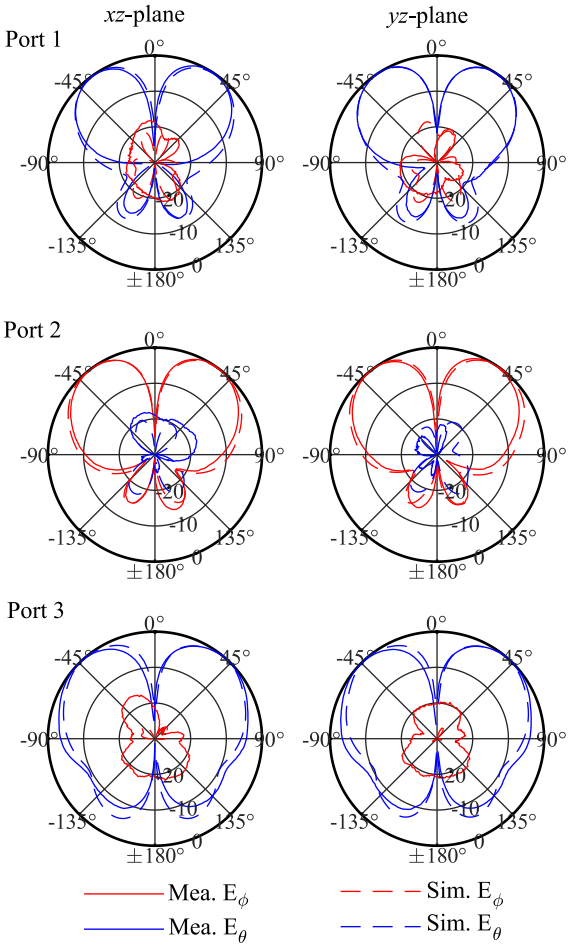

FIGURE 18. Normalized radiation patterns for Port 1, 2 and 3 excitation.

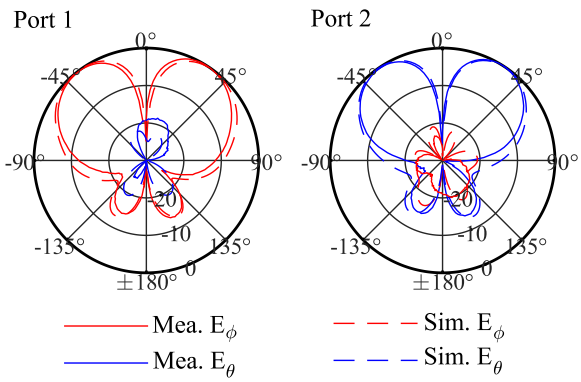

FIGURE 19. Normalized radiation patterns for Port 1, 2 excitation in the $\phi = 45^\circ$ plane.

is noted that the pattern for Port 4 and Port 6 have the same polarization. So for such pairs, (i.e., Port 4 & Port 6, Port 5 & Port 7) the high isolation is obtained by antenna spacing and the fact that each pattern points toward opposite directions.

Overall, the antenna achieves an overlapped impedance bandwidth of 7.7% (with $|S_{11}|$ better than -9.3 dB) and isolation better than 20 dB among all 7 ports. It should be emphasized that this isolation is achieved without using any additional decoupling structures. The isolation is obtained mainly due to the orthogonality of the radiation patterns. Furthermore, while decoupling structures can work very well in the case of two or three antennas [40], [41], [42], it might be critically challenging to design such decoupling structures simultaneously working for a large number of ports within a compact structure as demonstrated in this paper.

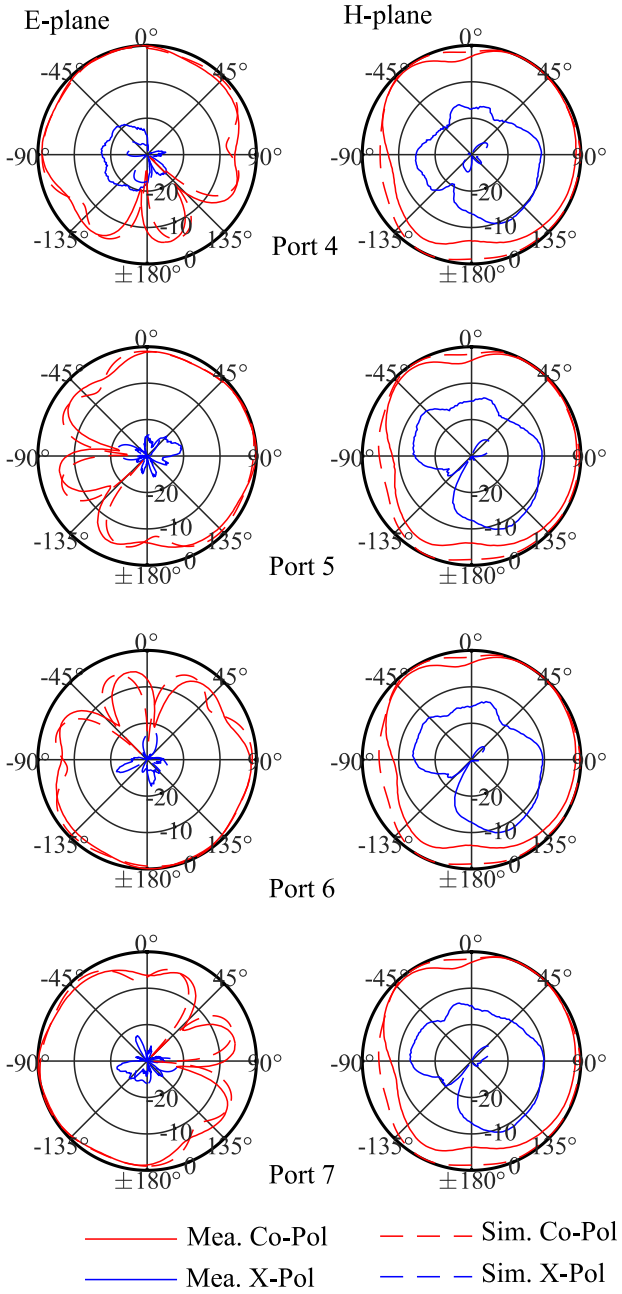

FIGURE 20. Normalized radiation patterns for Port 4, 5, 6, 7 excitation.

B. GAIN AND RADIATION PATTERNS

The normalized radiation patterns for Port 1, 2, 3 in the $\phi = 0°$ and $\phi = 90°$ plane are shown in Fig. 18. Very good agreement between simulation and measurement is obtained. The antenna has quite low cross polarization, i.e., better than about -20 dB with just a few exception where measured cross-pol is slightly larger mainly due to the imperfection of our anechoic chamber.

A quick glance at the 2D patterns in Fig. 18 suggests that all Port 1, 2 and 3 exhibit omnidirectional patterns while the patterns for Port 1 and Port 3 seem to be similar. However, only Port 3 provides an omnidirectional pattern with vertical polarization. As explained in Section III, the omnidirectionality for Port 1 and Port 2 is only applicable for the *total pattern*. The patterns for E_θ and E_ϕ (θ and ϕ component of antenna gain) are not omnidirectional. The radiation patterns for these two ports at $\phi = 45°$ are shown in Fig. 19, which confirms the theory and prediction shown in Section III.

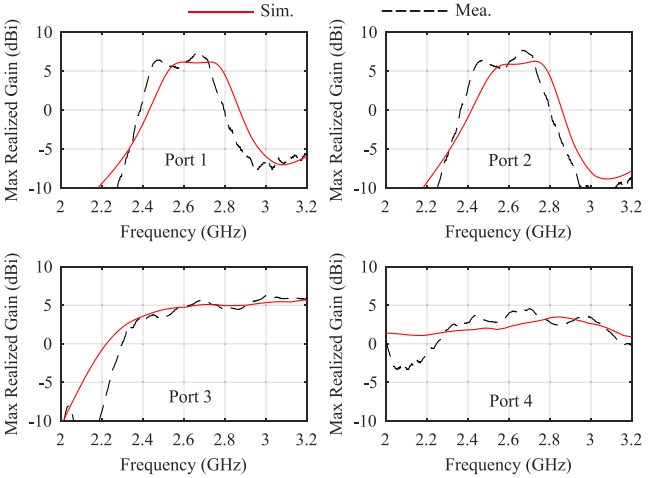

FIGURE 21. Simulated and measured realized gain for Port 1-4 excitation.

Finally, the radiation patterns for the E-plane and H-plane of the dipoles excited from Port 4-7 are shown in Fig. 20. For Port 4-7, the E-plane is the xy-plane or $\theta = 90°$-plane. The H-plane corresponds to $\phi = -22.5°, 67.5°, 157.5°, 247.5°$ for Port 4, 5, 6, and 7 respectively. Good agreement between simulations and measurements is observed. The antenna can radiate a horizontally polarized broad beam with maxima towards different angles $\phi = -22.5°, 67.5°, 157.5°, 247.5°$ corresponding to Port 4, 5, 6, and 7 excitation. For E-plane measurement, low measured cross-polarization is obtained which agrees well with simulation predictions. However, the measurement on the H-plane shows higher cross polarization (even at $\theta = 90°$). Thus, the high measured cross-polarization in the H-plane is likely due to the imperfection of measurement in the chamber, e.g., the effect of the antenna stand.

All patterns in the H-plane indicate that the broadside direction ($\theta = 0°$) is also covered with polarization diversity, i.e., linear polarization with electric field in the direction of $\phi = -22.5°, 67.5°, 157.5°, 247.5°$, with a gain dropping by just about 2-3 dB compared to the maximum gain.

Finally, the measured and simulated maximum realized gain for Port 1-4 excitation are shown in Fig. 21. The results for Port 5, 6 and 7 are almost identical with that of Port 4 and not shown here for brevity. Good agreement with simulations is generally observed at all ports. It is noted that the operating frequency is slightly shifted to the left for Port 1 and 2 excitation (see Fig. 13), which can also be observed in the gain profile. The slightly higher gain in measurement compared to simulation is attributed to the imperfection of our chamber: the multipath effects can cause some ripples

TABLE 1. Summary of measured results for all ports of the proposed antenna.

Port	−10-dB Bandwidth	Total Gain Pattern	Polarization & Max. Gain Direction	Max. Realized Gain
1	2.49 - 2.69 GHz	Ominidirectional	$G_\theta : \theta = \pm 40°, \phi = 0°, 90°$ $G_\phi : \theta = \pm 40°, \phi = -45°, 45°$	7.4 dBi
2	2.49 - 2.69 GHz	Ominidirectional	$G_\theta : \theta = \pm 40°, \phi = -45°, 45°$ $G_\phi : \theta = \pm 40°, \phi = 0°, 90°$	7.6 dB
3	2.39 - >3.20 GHz	Ominidirectional	$G_\theta : \theta = \pm 45°$	5.7 dBi
4	2.46 - 2.82 GHz	Unidirectional	$G_\phi : \theta = 90°, \phi = -22.5°$	4.5 dBi
5	2.44 - 2.78 GHz	Unidirectional	$G_\phi : \theta = 90°, \phi = 67.5°$	4.5 dBi
6	2.37 - 2.76 GHz	Unidirectional	$G_\phi : \theta = 90°, \phi = 157.5°$	4.5 dBi
7	2.42 - 2.78 GHz	Unidirectional	$G_\phi : \theta = 90°, \phi = 247.5°$	4.5 dBi

TABLE 2. Comparison between the proposed antenna and recent multi-port antennas in literature.

Ref.	**size** (λ_L^3)	**No. of Ports**	**Relative bandwidth**	**Minimum isolation (dB)**	**Coverage**	**Polarization Diversity**
[1]	$0.41 \times 0.41 \times \mathbf{0.41}$	6	5%	9 dB	3D space	Yes
[2]	$2.0 \times 1.7 \times \mathbf{0.46}$	6	21.2%	45 dB	Azimuth plane	No
[3]	$0.57^2 \times \pi \times \mathbf{0.14}$	6	80%	20 dB	Azimuth plane	No
[30]	$0.52^2 \times \pi \times \mathbf{0.061}$	4	6.5%	24.5 dB	Upper hemisphere	Yes
Proposed	$0.61^2 \times \pi \times \mathbf{0.061}$	7	7.7%	20 dB	Upper hemisphere	Yes

The isolation is quoted as the minimum value across the overlapped bandwidth.
λ_L is the free-space wavelength at the minimum operating frequency.

in gain, which may lead to a slight overestimation of the measured gain. The simulated efficiency is better than 95% for all ports across the overlapping impedance bandwidth, which is expected for a passive antenna at this frequency range. Based on the gain and pattern measurements, it is reasonably expected that the practical efficiency is also high. To summarize, the antenna performance for each port excitation is illustrated in Table 1.

C. DESIGN COMPARISON

The comparison of the designs with recent multi-port pattern-diversity antennas (with the number of ports at least 4) is shown in Table 2. It is noted that these antennas are quite distinct in number of ports (which crucially affect the isolation and antenna size), space coverage and polarization diversity. Thus, it is in general difficult to have a direct comparison. Nevertheless, one can observe that the proposed design exhibits a low-profile structure with the largest number of port while keeping relatively high isolation. It also covers the whole upper hemisphere (which suitable for applications such as vehicular platform integration) with polarization diversity.

VI. CONCLUSION

A seven-port pattern-diversity antenna has been presented in this paper. The concept of tripolarization has been generalized, which inspired an initial design with three orthogonal omnidirectional total gain patterns. Then four more ports have been added, which utilize both pattern orthogonality and antenna spacing to achieve high isolation. These four additional ports are designed to ensure a high degree of pattern/polarization diversity at any direction in the upper hemisphere space. An antenna prototype has been fabricated and measured, which confirm the theoretical prediction. For 7

ports, the antenna has a relative compact and low-profile structure with the size of $(0.61^2 \times \pi \times 0.061)\lambda_L^3$ where λ_L is the free-space wavelength at the lowest operating frequency. The antenna achieves an operating bandwidth of 7.7% from 2.49 GHz to 2.69 GHz. Across the bandwidth, the isolation between any two ports is better than 20 dB. It should also be noted that high isolation is achieved exploiting only the orthogonality of the pattern and antenna spacing, i.e., without any additional decoupling structures.

REFERENCES

[1] C. Chiu, J. Yan, R. D. Murch, J. X. Yun, and R. G. Vaughan, "Design and implementation of a compact 6-port antenna," *IEEE Antennas Wireless Propag. Lett.*, vol. 8, pp. 767–770, 2009.

[2] W. Han, X. Zhou, J. Ouyang, Y. Li, R. Long, and F. Yang, "A six-port MIMO antenna system with high isolation for 5-GHz WLAN access points," *IEEE Antennas Wireless Propag. Lett.*, vol. 13, pp. 880–883, 2014.

[3] K.-L. Wong, Z.-W. Tso, and W.-Y. Li, "Very-wide-band six-port single-patch antenna with six uncorrelated waves for MIMO access points," *IEEE Access*, vol. 10, pp. 69555–69567, 2022.

[4] M. R. Andrews, P. P. Mitra, and R. deCarvalho, "Tripling the capacity of wireless communications using electromagnetic polarization," *Nature*, vol. 409, pp. 316–318, Jan. 2001.

[5] C. Chiu, J. Yan, and R. D. Murch, "Compact three-port orthogonally polarized MIMO antennas," *IEEE Antennas Wireless Propag. Lett.*, vol. 6, pp. 619–622, Dec 2007.

[6] J. Sarrazin, Y. Mahe, S. Avrillon, and S. Toutain, "Investigation on cavity/slot antennas for diversity and MIMO systems: The example of a three-port antenna," *IEEE Antennas Wireless Propag. Lett.*, vol. 7, pp. 414–417, 2008.

[7] K. Tong, H. Tang, A. Al-Armaghany, and W. Hong, "Low-profile orthogonally tripolarized antennas," *IEEE Antennas Wireless Propag. Lett.*, vol. 12, pp. 876–879, 2013.

[8] L. Liu, C. Liu, Z. Li, X. Yin, and Z. N. Chen, "Slit-slot line and its application to low cross-polarization slot antenna and mutual-coupling suppressed tripolarized MIMO antenna," *IEEE Trans. Antennas Propag.*, vol. 67, no. 1, pp. 4–15, Jan. 2019.

[9] L. Zou and C. Fumeaux, "A cross-shaped dielectric resonator antenna for multifunction and polarization diversity applications," *IEEE Antennas Wireless Propag. Lett.*, vol. 10, pp. 742–745, 2011.

[10] X. S. Fang, K. W. Leung, and K. M. Luk, "Theory and experiment of three-port polarization-diversity cylindrical dielectric resonator antenna," *IEEE Trans. Antennas Propag.*, vol. 62, no. 10, pp. 4945–4951, Oct. 2014.

[11] K. Wei, Z. Zhang, W. Chen, and Z. Feng, "A novel hybrid-fed patch antenna with pattern diversity," *IEEE Antennas Wireless Propag. Lett.*, vol. 9, pp. 562–565, 2010.

[12] N. P. Lawrence, C. Fumeaux, and D. Abbott, "Planar triorthogonal diversity slot antenna," *IEEE Trans. Antennas Propag.*, vol. 65, no. 3, pp. 1416–1421, Mar. 2017.

[13] X. Gao, H. Zhong, Z. Zhang, Z. Feng, and M. F. Iskander, "Low-profile planar tripolarization antenna for WLAN communications," *IEEE Antennas Wireless Propag. Lett.*, vol. 9, pp. 83–86, 2010.

[14] K. Saurav, N. K. Mallat, and Y. M. M. Antar, "A three-port polarization and pattern diversity ring antenna," *IEEE Antennas Wireless Propag. Lett.*, vol. 17, no. 7, pp. 1324–1328, Jul. 2018.

[15] D. Piao and Y. Wang, "Tripolarized MIMO antenna using a compact single-layer microstrip patch," *IEEE Trans. Antennas Propag.*, vol. 67, no. 3, pp. 1937–1940, Mar. 2019.

[16] D. Piao and Y. Wang, "Experimental evaluation of the tri-polarized MIMO channel properties based on a compact multimode antenna," *IEEE Access*, vol. 7, pp. 67807–67817, 2019.

[17] D. Piao, M. Wang, J. Zuo, L. Zhang, and Y. Wang, "Compact and low-coupled tripolarized microstrip MIMO antenna based on parasitic patch loading," *IEEE Trans. Antennas Propag.*, vol. 69, no. 9, pp. 5992–5997, Sep. 2021.

[18] Y. Zhang, K. Wei, Z. Zhang, and Z. Feng, "A broadband patch antenna with tripolarization using quasi-cross-slot and capacitive coupling feed," *IEEE Antennas Wireless Propag. Lett.*, vol. 12, pp. 832–835, 2013.

[19] N. Nguyen-Trong, S. X. Ta, M. Ikram, K. Bertling, and A. M. Abbosh, "A low-profile wideband tripolarized antenna," *IEEE Trans. Antennas Propag.*, vol. 67, no. 3, pp. 1946–1951, Mar. 2019.

[20] S. X. Ta, D. Nguyen-Thi, K. K. Nguyen, C. Dao-Ngoc, and N. Nguyen-Trong, "Design of a low-profile tripolarized antenna with wide bandwidth," *IEEE Access*, vol. 7, pp. 82701–82708, 2019.

[21] Z. Wang, S. Liu, and Y. Dong, "Low-profile metasurface-based antenna with tripolarization for 5G applications," *IEEE Trans. Antennas Propag.*, vol. 69, no. 9, pp. 5437–5445, Sep. 2021.

[22] L. Y. Nie, B. K. Lau, H. Aliakbari, S. Xiang, B. Wang, and X. Q. Lin, "A low-profile wideband dual-resonance tri-port MIMO antenna," *IEEE Trans. Antennas Propag.*, vol. 70, no. 6, pp. 4866–4871, Jun. 2022.

[23] S. X. Ta, D. M. Nguyen, K. K. Nguyen, C. Dao-Ngoc, and N. Nguyen-Trong, "A tripolarized antenna with ultrawide operational bandwidth," *IEEE Trans. Antennas Propag.*, vol. 68, no. 6, pp. 4386–4396, Jun. 2020.

[24] S. Yan and G. A. E. Vandenbosch, "Wearable antenna with tripolarisation diversity for WBAN communications," *Electron. Lett.*, vol. 52, no. 7, pp. 500–502, 2016.

[25] K. Zhang, Z. H. Jiang, W. Hong, and D. H. Werner, "A low-profile and wideband triple-mode antenna for wireless body area network concurrent on-/off-body communications," *IEEE Trans. Antennas Propag.*, vol. 68, no. 3, pp. 1982–1994, Mar. 2020.

[26] Y. Wang, D. Piao, and J. Zuo, "A wide-angle and fully polarimetric retrodirective array based on tri-polarized antennas with pattern complementation," *IEEE Trans. Antennas Propag.*, vol. 70, no. 6, pp. 4518–4525, Jun. 2022.

[27] B. Feng, J. Chen, S. Yin, C.-Y.-D. Sim, and Z. Zhao, "A tri-polarized antenna with diverse radiation characteristics for 5G and V2X communications," *IEEE Trans. Veh. Technol.*, vol. 69, no. 9, pp. 10115–10126, Sep. 2020.

[28] R. Vaughan and J. Andersen, "Antenna diversity in mobile communications," *IEEE Trans. Veh. Technol.*, vol. 36, no. 4, pp. 149–172, Nov. 1987.

[29] S. Blanch, J. Romeu, and I. Corbella, "Exact representation of antenna system diversity performance from input parameter description," *Electron. Lett.*, vol. 39, no. 9, pp. 705–707, May 2003.

[30] Y. Wen, D. Yang, H. Zeng, M. Zou, and J. Pan, "Bandwidth enhancement of low-profile microstrip antenna for MIMO applications," *IEEE Trans. Antennas Propag.*, vol. 66, no. 3, pp. 1064–1075, Mar. 2018.

[31] S.-J. Lin and J.-S. Row, "Monopolar patch antenna with dual-band and wideband operations," *IEEE Trans. Antennas Propag.*, vol. 56, no. 3, pp. 900–903, Mar. 2008.

[32] N. Nguyen-Trong, A. Piotrowski, T. Kaufmann, and C. Fumeaux, "Low-profile wideband monopolar UHF antennas for integration onto vehicles and helmets," *IEEE Trans. Antennas Propag.*, vol. 64, no. 6, pp. 2562–2568, Jun. 2016.

[33] H. Nakano, H. Iwaoka, K. Morishita, and J. Yamauchi, "A wideband low-profile antenna composed of a conducting body of revolution and a shorted parasitic ring," *IEEE Trans. Antennas Propag.*, vol. 56, no. 4, pp. 1187–1192, Apr. 2008.

[34] L. Zou, D. Abbott, and C. Fumeaux, "Omnidirectional cylindrical dielectric resonator antenna with dual polarization," *IEEE Antennas Wireless Propag. Lett.*, vol. 11, pp. 515–518, 2012.

[35] X. Quan and R. Li, "A broadband dual-polarized omnidirectional antenna for base stations," *IEEE Trans. Antennas Propag.*, vol. 61, no. 2, pp. 943–947, Feb. 2013.

[36] Y. Fan, X. Liu, B. Liu, and R. Li, "A broadband dual-polarized omnidirectional antenna based on orthogonal dipoles," *IEEE Antennas Wireless Propag. Lett.*, vol. 15, pp. 1257–1260, 2016.

[37] S. X. Ta, D. M. Nguyen, K. K. Nguyen, C. Dao-Ngoc, and N. Nguyen-Trong, "Dual-polarized omnidirectional antenna with simple feed and ultrawide bandwidth," *IEEE Antennas Wireless Propag. Lett.*, vol. 19, no. 5, pp. 871–875, May 2020.

[38] H. Huang, Y. Liu, and S. Gong, "Broadband dual-polarized omnidirectional antenna for 2G/3G/LTE/WiFi applications," *IEEE Antennas Wireless Propag. Lett.*, vol. 15, pp. 576–579, 2016.

[39] H. Gu, L. Ge, and J. Zhang, "A dual-band dual-polarized omnidirectional antenna," *Front. Phys.*, vol. 8, Dec. 2020, Art. no. 614911. [Online]. Available: https://www.frontiersin.org/articles/10.3389/fphy.2020.614911

[40] K. Wei, J.-Y. Li, L. Wang, Z.-J. Xing, and R. Xu, "Mutual coupling reduction by novel fractal defected ground structure bandgap filter," *IEEE Trans. Antennas Propag.*, vol. 64, no. 10, pp. 4328–4335, Oct. 2016.
[41] M.-C. Tang et al., "Mutual coupling reduction using meta-structures for wideband, dual-polarized, and high-density patch arrays," *IEEE Trans. Antennas Propag.*, vol. 65, no. 8, pp. 3986–3998, Aug. 2017.
[42] A. A. Ghannad, M. Khalily, P. Xiao, R. Tafazolli, and A. A. Kishk, "Enhanced matching and vialess decoupling of nearby patch antennas for MIMO system," *IEEE Antennas Wireless Propag. Lett.*, vol. 18, no. 6, pp. 1066–1070, Jun. 2019.

NGHIA NGUYEN-TRONG (Senior Member, IEEE) received the Ph.D. degree (Doctoral Research Medal) in electrical engineering from The University of Adelaide, Adelaide, SA, Australia, in 2017.

From 2017 to 2020, he was a Postdoctoral Researcher with The University of Queensland, Brisbane, QLD, Australia. Since 2021, he has been a Lecturer with The University of Adelaide. His main research interests include microwave circuits, advanced materials, absorbers, and various types of antennas.

Dr. Nguyen-Trong was one of the recipients of the Best Student Paper Award at the 2014 IWAT, the 2015 IEEE MTT-S NEMO, and the 2017 ASA Conferences, and the Best Paper Award at the 2018 and 2020 Australian Microwave Symposium Conferences. He has been continuously selected as a Top Reviewer for IEEE TRANSACTIONS ON ANTENNAS AND PROPAGATION from 2018 to 2021 and IEEE ANTENNA WIRELESS AND PROPAGATION LETTERS in 2018 and 2021. He serves as the Technical Co-Chair for the 2020, 2023 AMS, and 2022 IEEE International Symposium on Antennas and Propagation. He is listed among Australia's Top 40 Early Career Researchers by The Australian, November 2021.

CHRISTOPHE FUMEAUX (Fellow, IEEE) received the Diploma and Ph.D. degrees in physics from ETH Zurich, Switzerland, in 1992 and 1997, respectively.

From 1998 to 2000, he was a Postdoctoral Researcher with the School of Optics, University of Central Florida, Orlando. In 2000, he joined the Swiss Federal Office of Metrology, Bern, Switzerland, as a Scientific Staff Member. From 2001 to 2008, he was a Research Associate and a Lecturer with the Laboratory for Electromagnetic Fields and Microwave Electronics, ETH Zurich. From 2008 to 2023, he was a Professor with The University of Adelaide, Australia. In 2023, he joined the School of Electrical Engineering and Computer Science, The University of Queensland as the Chair Professor of Optical and Microwave Engineering. His main research interests concern applied electromagnetics, antenna engineering, and the application of RF design principles across the electromagnetic spectrum.

Prof. Fumeaux was the recipient of the ETH Medal for his doctoral dissertation. He was the recipient of the 2018 Edward E. Altshuler Prize, the 2014 IEEE SENSORS JOURNAL, and the 2004 *Applied Computational Electromagnetics Society* Best Paper Awards. He also received Best Conference Paper Awards at the 2012 Asia–Pacific International Symposium on Electromagnetic Compatibility and the 17th Colloque International sur la Compatibilité Electromagnétique in 2014. More than ten of his students have received student awards with joint papers at IEEE conferences. He was the recipient of the University of Adelaide Stephen Cole the Elder Award for Excellence in Higher Degree by Research Supervisory Practice in 2018. He served as an Associate Editor for the IEEE TRANSACTIONS ON MICROWAVE THEORY AND TECHNIQUES from 2010 to 2013. From 2013 to 2016, he served as a Senior Associate Editor and later as the Associate Editor-in-Chief for the IEEE TRANSACTIONS ON ANTENNAS AND PROPAGATION. From 2017 to early 2023, he served as the Editor-in-Chief for the IEEE ANTENNAS AND WIRELESS PROPAGATION LETTERS. From 2011 to 2015, he was a Future Fellow of the Australian Research Council.